Article

Crustal structure beneath the Hi-CLIMB seismic array in the central-western Tibetan Plateau from the improved *H*-*κ*-c method

Jiangtao Li[1,✉], and Xiaodong Song[2,✉]

[1] *Department of Geophysics*, *School of Geodesy and Geomatics*, *Wuhan University*, *Wuhan* 430079, *China*
[2] *Institute of Theoretical and Applied Geophysics*, *School of Earth and Space Sciences*, *Peking University*, *Beijing* 100871, *China*

Corresponding author Li JT, email: jiangtaoli@whu.edu.cn; Song XD, email: xdsong@pku.edu.cn

Key points:

- Application of the *H*-*κ*-c method on the Hi-CLIMB array demonstrates that it works well for regions with complex crustal structures.
- The two regions observed with high crustal v_P/v_S correlate with mid-crust low S velocities, suggesting possible presence of partial melt.
- The Lhasa block has relatively lower crustal v_P/v_S and relatively higher crustal S velocity, which is interpreted to be mechanically stronger than the Himalaya and Qiangtang blocks.

Abstract The Hi-CLIMB seismic array is located in the central-western Tibetan Plateau. The *H*-*κ*-c method (Li JT et al., 2019) was applied to receiver function data on the Hi-CLIMB, which corrects the back-azimuthal variations in the arrival times of Ps and crustal multiples caused by crustal anisotropy and dipping interfaces before performing *H*-*κ* stacking. Compared to the traditional *H*-*κ* method, the *H*-*κ* stacking results after harmonic corrections showed considerable improvements, including greatly reduced errors, significantly less scattered *H* (crustal thickness) and *κ* (crustal v_P/v_S ratio) values, and clearer patterns of *H* and *κ* in different Tibetan blocks. This demonstrates that the *H*-*κ*-c method works well even for regions with complex crustal structures, such as the Tibetan Plateau, when there are helpful references from nearby stations or other constraints. The variation in crustal thickness agrees with previous studies but tends to be relatively shallower beneath most of the plateau. Two regions with particularly high crustal v_P/v_S were observed, namely, one in the northern Himalaya block and beneath the Yarlung-Zangbo suture, and the other in the Qiangtang block. Their correlation with mid-crust low S velocities from previous studies suggests the possible presence of fluid or partial melt in the two regions, which may have implications for the crustal flow model. In contrast, the Lhasa block had relatively lower crustal v_P/v_S and relatively higher crustal S velocity within the plateau, which is interpreted to be mechanically stronger than the Himalaya and Qiangtang blocks, and without mid-crust partial melt.

Keywords: *H*-*κ*-c method; receiver function; Hi-CLIMB; crustal thickness; crustal v_P/v_S ratio.

Citation: Li JT, and Song XD (2021). Crustal structure beneath the Hi-CLIMB seismic array in the central-western Tibetan Plateau from the improved *H*-*κ*-c method. Earthq Sci **34**, doi: 10.29382/eqs-2021-0002

1. Introduction

The crustal thickness (*H*) and crustal v_P/v_S ratio (*κ*) are important parameters for understanding regional geology and tectonic evolution. The receiver function *H*-*κ* stacking method developed by Zhu LP and Kanamori (2000) has been widely used to estimate *H* and *κ* through a grid search. It stacks the amplitudes of receiver functions at predicted arrival times of Ps converted phase and its crustal multiples (PpPs and PpSs + PsPs) for given values of *H* and *κ*, which reduces the trade-off between *H* and *κ*. However, the method assumes an isotropic crust with a flat Moho, which is not often the case. In the presence of a complex crustal structure and insufficient data coverage,

Received 13 February 2021; **received in revised form** 6 May 2021; **accepted** 11 May 2021; **available online** 2 June 2021.

the *H*-κ results may be biased (Li JT et al., 2017, 2019). Synthetic tests with crustal anisotropy and dipping layers also revealed that the influence on the variations in arrival times of crustal multiples is even stronger than on those of Ps, and this would affect the *H*-κ estimates (e.g., Li JT et al., 2017, 2019).

To mitigate this problem, Li JT et al. (2019) proposed a generalized version of the *H*-κ stacking method (Zhu LP and Kanamori, 2000) with harmonic corrections (*H*-κ-c, where "c" stands for "correction"), which considered rather general cases of crustal structures, including plunging anisotropy (anisotropy with tilted symmetry axis from the horizontal plane) and dipping interfaces of multiple layers. The key idea of the *H*-κ-c method (Li JT et al., 2019) is to use cosθ (two-lobed) and cos2θ (four-lobed) functions (e.g., Cassidy, 1992; Levin and Park, 1997a, b; Savage, 1998; Frederiksen and Bostock, 2000; Liu HF and Niu FL, 2012; Rümpker et al., 2014) to correct the back-azimuthal variations in the arrival times of both Ps and crustal multiples, for the complicated effects of crustal anisotropy and dipping interfaces, and then perform traditional *H*-κ stacking (Zhu LP and Kanamori, 2000). Both the synthetic tests and application to 40 Chinese National Digital Seismic Network stations (Li JT et al., 2019) showed considerable improvement, with clearer crustal multiples and stronger stacking energy in *H*-κ, as well as more robust and reliable *H* and κ values. The improved estimation of the crustal v_P/v_S ratio (κ) can provide critical constraint on the composition and thermal condition of the crust (Li JT et al., 2019). The *H*-κ-c method has also been applied in South China (Deng YF et al., 2019) and Tien Shan (Zhang BF et al., 2020), demonstrating its wide applicability.

As mentioned by Li JT et al. (2019), special care needs to be taken when performing *H*-κ-c in regions such as the Tibetan Plateau (TP), where the crustal structure is particularly complicated. For example, two permanent stations (CAD and SQH) in the Tibetan Plateau displayed ambiguous *H*-κ results despite harmonic corrections (Li JT et al., 2019, their Supplementary Figure S11). The main reason lies in the crustal multiples (especially PpPs), which are either too weak or have several nearby peaks due to complicated structures. For these stations, visual inspections of the harmonic fittings and *H*-κ stacks, as well as references to nearby stations or other constraints, are helpful in judging the quality of the results (Li JT et al., 2019).

The TP is the largest and highest plateau on Earth. It was created by the Cenozoic Indian-Eurasian continental collision (Molnar and Tapponnier, 1975; Yin and Harrison, 2000). Despite decades of studies, controversy remains over the basic aspects of its geology. Various hypotheses and models have been proposed for the uplift and growth of the TP, such as underthrusting of the Indian lithosphere beneath Tibet (Powell, 1986; Owens and Zandt, 1997), eastward rigid-block extrusion (Molnar and Tapponnier, 1975; Tapponnier et al., 2001), continuous deformation (England and Houseman, 1986; Zhang PZ et al., 2004), and mid-lower crustal flow (Clark and Royden, 2000; Royden et al., 1997, 2008; Klemperer, 2006). Better constrained crustal models, such as thickness, velocity, and v_P/v_S ratio, can be useful for examining these hypotheses.

The Himalayan-Tibetan Continental Lithosphere during Mountain Building (Hi-CLIMB) seismic array is located in the central-western TP, and extends from the Ganga foreland in the south, through the Himalaya and Lhasa blocks, and reaches the central Qiangtang block (Figure 1). From 2002 to 2005, and with a length of over 700 km, the network included 75 broadband seismic stations from the U.S. Program for Array Seismic Studies of the Continental Lithosphere (PASSCAL), supplemented in southern Tibet by 32 stations from Peking University and the Chinese Academy of Geological Sciences, China, and from the Academia Sinica, China (Nábělek et al., 2009). Although the details vary, previous studies on Hi-CLIMB have shared a similar pattern of Moho variation, increasing from ~40–50 km in the south to ~70–75 km in the Lhasa block, and then gradually decreasing to ~60–65 km in the Qiangtang block (Nábělek et al., 2009; Tseng et al., 2009; Wittlinger et al., 2009; Nowack et al., 2010; Xu ZJ et al., 2013a). Nábělek et al. (2009) suggested that the crust-mantle interface beneath Tibet is anisotropic, indicating shearing during its formation. Xu ZJ et al. (2013a) performed a joint inversion of the receiver function and surface wave dispersion on Hi-CLIMB and revealed discontinuous patches of low-velocity zones in the mid-crust, especially two patches in the Himalaya block near the Yarlung-Zangbo suture (YZS) and within the Qiangtang block, respectively. Their correlation with low electric resistivity (Unsworth et al., 2005) might suggest the presence of fluid or partial melt (Xu ZJ et al., 2013a).

In this study, the *H*-κ-c method (Li JT et al., 2019) was applied to receiver function data on the dense Hi-CLIMB seismic array. The Hi-CLIMB array was chosen for the following reasons. (1) It is located in the Tibetan Plateau, where the crust is the world's most complicated. (2) It has good data quality and has been well studied (Nábělek et al., 2009; Tseng et al., 2009; Wittlinger et al., 2009; Chen WP et al., 2010; Nowack et al., 2010; Xu Q et al., 2011; Xu ZJ et al., 2013a; Zhou YM, 2013; Duputel et al., 2016; Shang XF et al., 2017). (3) As a dense north-south profile with an average station interval of ~5 km (Nábělek et al.,

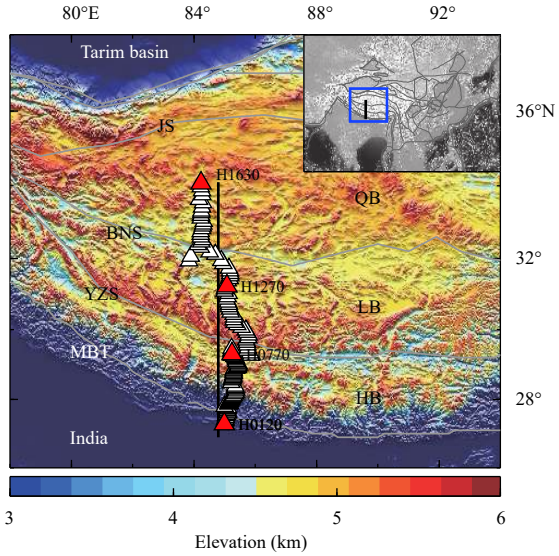

Figure 1. Topographic map and distribution of the Hi-CLIMB stations used in this study. Inset shows its location (blue box) in East and South Asia with topography (gray). White triangles indicate the positions of the seismic stations with four example stations (Figures 2–5) shown in red. The black line is the projection line of the profile as shown in Figures 6, 8, and 9. The gray lines mark the major block boundaries. BNS: Bangong-Nujiang suture; HB: Himalaya block; JS: Jinsha suture; LB: Lhasa block; MBT: Main Boundary Thrust; QB: Qiangtang block; YZS: Yarlung-Zangbu suture.

2009), nearby stations can provide good references for each other when one station has ambiguous solutions. (4) As a profile cutting across several Tibetan blocks, the crustal structure beneath the Hi-CLIMB is important to study with various methods. The main purposes of this study were to obtain the crustal structure beneath the Hi-CLIMB array and to test the adaptability of the *H*-*κ*-c method for complicated crustal structures.

2. Data and method

Tele-seismic P-wave receiver functions (RFs) were originally computed by Zhou YM, (2013) and were later used in Xu ZJ et al. (2013a). The RFs were constructed following a routine procedure (Zhu LP and Kanamori, 2000) using the time domain iterative deconvolution method (Ligorria and Ammon, 1999), with a Gaussian parameter of 3.0. Of the 145 Hi-CLIMB stations with RF data, 23 stations were discarded for the following reasons. (1) The first 10 stations (H0010 to H0100), due to a very thick sedimentary layer that can be seen from the beginning part of the RFs (the peak is at ~2 s but not ~0 s), which would significantly affect the *H*-*κ* (e.g., Li JT et al., 2017). (2) Ten stations, namely, H0180, H0230, H0520, H0530, H0550, H1350, H1380, H1390, H1423, and H1425, due to back-azimuthal gaps larger than 90° in RFs to ensure the recovery of cos2θ feature (Rümpker et al., 2014). (3) Three stations, namely, H0200, H1410, and H1421, due to an ambiguous Ps phase even with reference to nearby stations, which would make the results unreliable. The final number of RF stations was 122 (Figure 1).

The *H*-*κ*-c method includes the following four main steps: (1) Apply the traditional *H*-*κ* stacking (Zhu LP and Kanamori, 2000) to obtain the reference arrival times for Ps and crustal multiples; (2) perform incidence moveout corrections (Yuan XH et al., 1997) and 5° back-azimuthal binning on all the RFs; (3) obtain harmonic fits of the back-azimuthal variations of Ps and crustal multiples; (4) perform *H*-*κ*-c: use the parameters from (3) to correct the RFs of Ps and multiples and redo *H*-*κ* stacking with the corrected RFs (Li JT et al., 2019). For most of the stations used in Li JT et al. (2019), running through the steps once was sufficient. However, special care is required for stations in regions with complex crustal structures, such as the Tibetan Plateau. Possible issues include (a) the traditional *H*-*κ* stacking may not provide appropriate reference arrival times; (b) for some stations, there may be other strong signals before or after the Ps phase; and more often (c) the crustal multiples are either too weak or have several peaks within a few seconds.

For these cases, visual inspections with reference to nearby stations or other constraints were incorporated into the *H*-*κ*-c method. The principle was to determine the Ps phase first, and then ensure the crustal multiples. Steps (1), (2), and (4) were the same, while step (3) was developed into five detailed steps:

(3-1) Run harmonic fitting for Ps phase using reference from traditional *H*-*κ* results.

(3-2) Check the fitting results for Ps, and correct those that are apparently wrong, for example, Ps arrival before 4 s or after 12 s, or Ps after 8 s for stations at low elevation (south of ~28° N), or Ps before 6 s for stations in the Lhasa or Qiangtang blocks.

(3-3) For stations with two or even three alternative Ps arrivals, pick the most possible one with reference to nearby Hi-CLIMB stations, sometimes referring to other studies (e.g., Nábělek et al., 2009; Xu ZJ et al., 2013a).

(3-4) Update the input file of reference *H* and *κ* after the above inspections and use it to run harmonic fitting for crustal multiples.

(3-5) Check the fitting results for two crustal multiples (especially for PpPs because it is assigned a weighting of 0.4 in *H*-*κ*-c stacking), and re-run the stations with ambiguous solutions with further updated references from

nearby stations. A rule of thumb is that the adjacent stations with similar Ps arrival time should not have a difference of larger than 3 s in the arrival times of crustal multiples.

The equation for the harmonic fitting is

$$F(\theta) = A_0 + A_1\cos(\theta-\theta_1) - A_2\cos2(\theta-\theta_2), \quad (1)$$

where $F(\theta)$ represents the variation of arrival times with back-azimuth (θ) for Ps or crustal multiples, A_0 is the central arrival time, and A_1, A_2, θ_1, and θ_2 are the amplitudes and phases of the two-lobed and four-lobed variations (Li JT et al., 2019). In real Earth, the crust may have several layers with different anisotropy or dipping, so the parameters A_1, A_2, θ_1, and θ_2 would represent the integrated effect of the crust. As mentioned in Li JT et al. (2019), higher orders, for example, cos3θ, can always be included for complicated structures. However, tests with higher-order harmonic fits have shown that the inclusion is not worthy of further effort because of added computational cost and insignificant improvement in H-κ results (Li JT et al., 2019). A simple grid-search method was used to perform the harmonic fitting, aiming to find the best solution for five parameters (d_t=A_0–t_{ref}, A_1, A_2, θ_1, and θ_2, where t_{ref} is the reference arrival time from traditional H-κ). The default search ranges were: d_t, –1.0 s to 1.0 s; A_1 and A_2, 0 s to 0.5 s for Ps, and 0 s to 0.75 s for crustal multiples; θ_1, 0° to 355°; θ_2, 0° to 175°.

The weightings for H-κ stacking were 0.7 (Ps), 0.2 (PpPs, or M1 for convenience), and 0.1 (PpSs + PsPs, or M2) before harmonic corrections (Zhu LP and Kanamori, 2000), and 0.5, 0.4, and 0.1 after corrections. The weighting of M1 was increased because the harmonic corrections enhanced the coherency of the M1 phase as well as the stacking energy, while keeping the weighting of M2 the same because it was relatively weaker and more complicated, especially for regions such as the TP (Li JT et al., 2019). The default search ranges of H and κ were 30–80 km and 1.6–2.0, respectively. A reference crustal P velocity of 6.3 km/s was used in the H-κ stacking (Zhu LP and Kanamori, 2000) because it hardly affects the results of H and κ.

3. Results and discussion

3.1. Example stations

Figures 2–5 illustrate the H-κ-c process and the characteristics of the different blocks, with four example stations displayed. Station H0120 is in the Ganga foreland south of the Main Boundary Thrust (MBT), H0770 is in the northern Himalaya block, H1270 is in the central Lhasa block, and H1630 is in the central Qiangtang block. All four stations show a good fit for Ps and M1 (panels a and b), although the M2 is not as clear or definite as Ps/M1 (panels c). However, this is not of concern because its weighting is only 0.1 (Li JT et al., 2019). Among the four stations, the fitting curves for M1 at H0120 (Figure 2b) and H1630 (Figure 5b) should be the only solution for the consistency and strong energy, while at H0770 (Figure 3b) and H1270 (Figure 4b), the M1 energy is not as significant. However, it is considered that they are the optimal solutions, primarily because of their consistent and relatively stronger energy, as well as some similarity with the Ps curves, although the Ps and M1 are not necessarily correlated (see explanations in Li JT et al., 2019).

Panels d and e in Figures 2–5 show the H-κ stacking results before (d) and after (e) harmonic corrections, respectively. The first observation is the improvement by clearer Ps and M1 traces as well as smaller errors, particularly for H0120 and H0770, where the errors are greatly reduced. In terms of H and κ values, at stations H0120 and H1630, they are similar before or after harmonic corrections; while at H0770 and H1270, the values have changed. For H0770, H increased by 5.0 km, and for H1270, H increased by 7.7 km while κ decreased by 0.07. In such cases, it is necessary to determine whether the values from H-κ-c are more reasonable. As shown in Figure 6, which summarizes all the stacking results, the κ values are more scattered than the H values either before or after corrections. Therefore, the trend of H variation and H at nearby stations after harmonic corrections are used as the main criteria. On this basis, it is found that a crustal thickness of 65.5 km (Figure 3e; closer to the average trend in Figure 6a) is more plausible than 60.5 km (Figure 3d) for H0770. For H1270, 62.4 km (Figure 4d) is too thin compared to the average trend and nearby stations (Figure 6a), and therefore, 70.1 km/1.71 (Figure 4e) would be a more reliable solution.

3.2. Crustal thickness

The results of H and κ values, as well as their errors from H-κ-c, are summarized in Figures 6 and 7, respectively. The standard deviations of H and κ of the 122 Hi-CLIMB stations are reduced from an average of ~3.84 km and ~0.060 to an average of ~2.35 km and ~0.042, corresponding to ~63% and ~51% variance reduction in H and κ, respectively (Figure 7). This validates the robustness of the H-κ-c method.

The values of crustal thickness (H) before, and after, harmonic corrections are indicated in Figure 6. It is apparent that the H values after corrections are

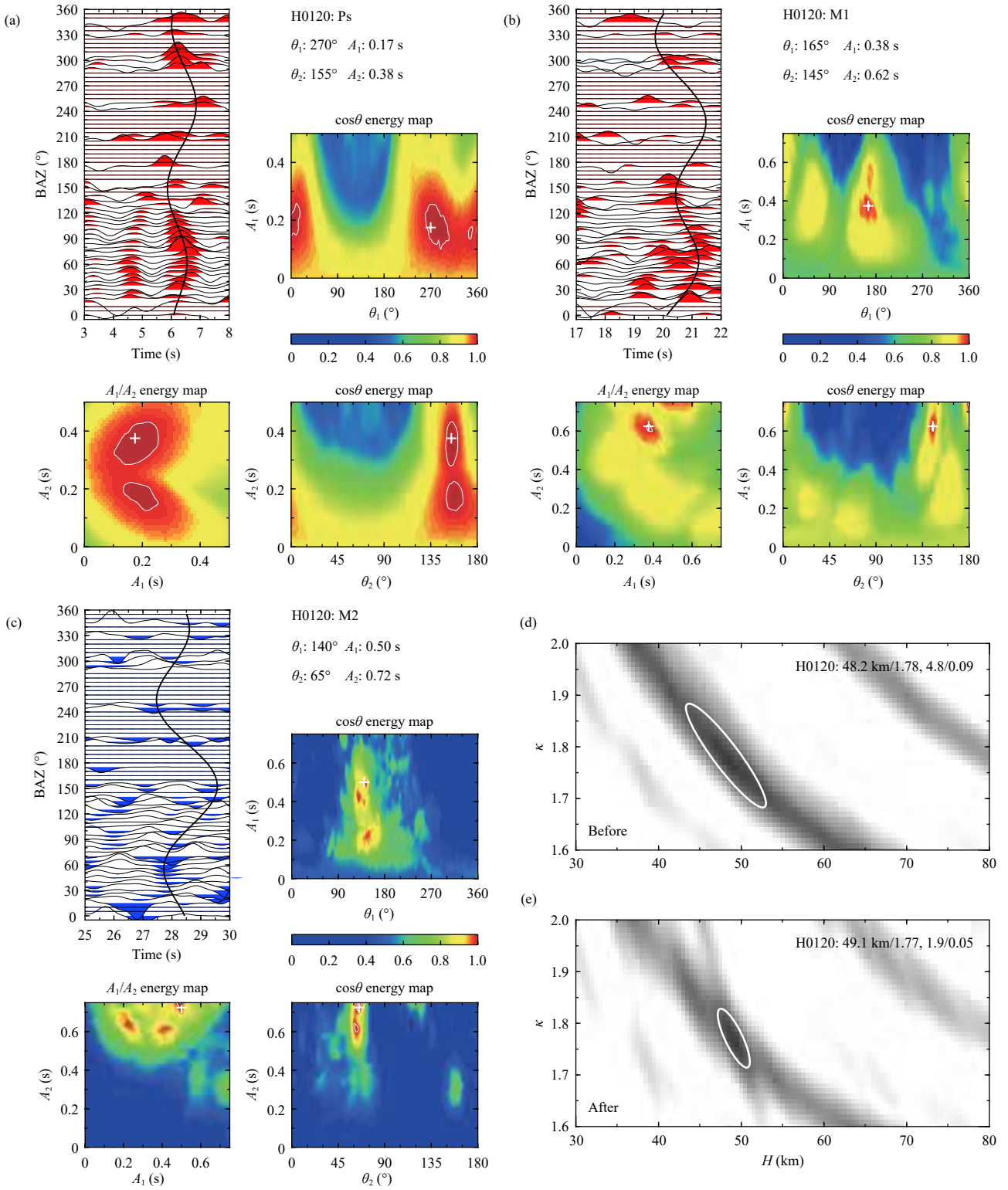

Figure 2. *H*-*κ*-c results on example station H0120. (a–c) Harmonic fitting results for Ps (a), M1 (b), and M2 (c), showing the fitting curves with cosθ and cos2θ functions, energy stacking maps of the grid search for harmonic parameters, and the search results. BAZ = back azimuth. The 99% contour is plotted in each energy map to show the empirical uncertainty. (d–e) *H*-*κ* stacking before (d) and after (e) the harmonic corrections. The weightings of Ps, M1, and M2 are 0.7, 0.2, and 0.1 in the traditional *H*-*κ* in (d), and 0.5, 0.4, and 0.1 in the *H*-*κ*-c after harmonic corrections in (e), respectively. The obtained *H* and *κ* values, their errors, and the error ellipse are shown in the stack diagrams.

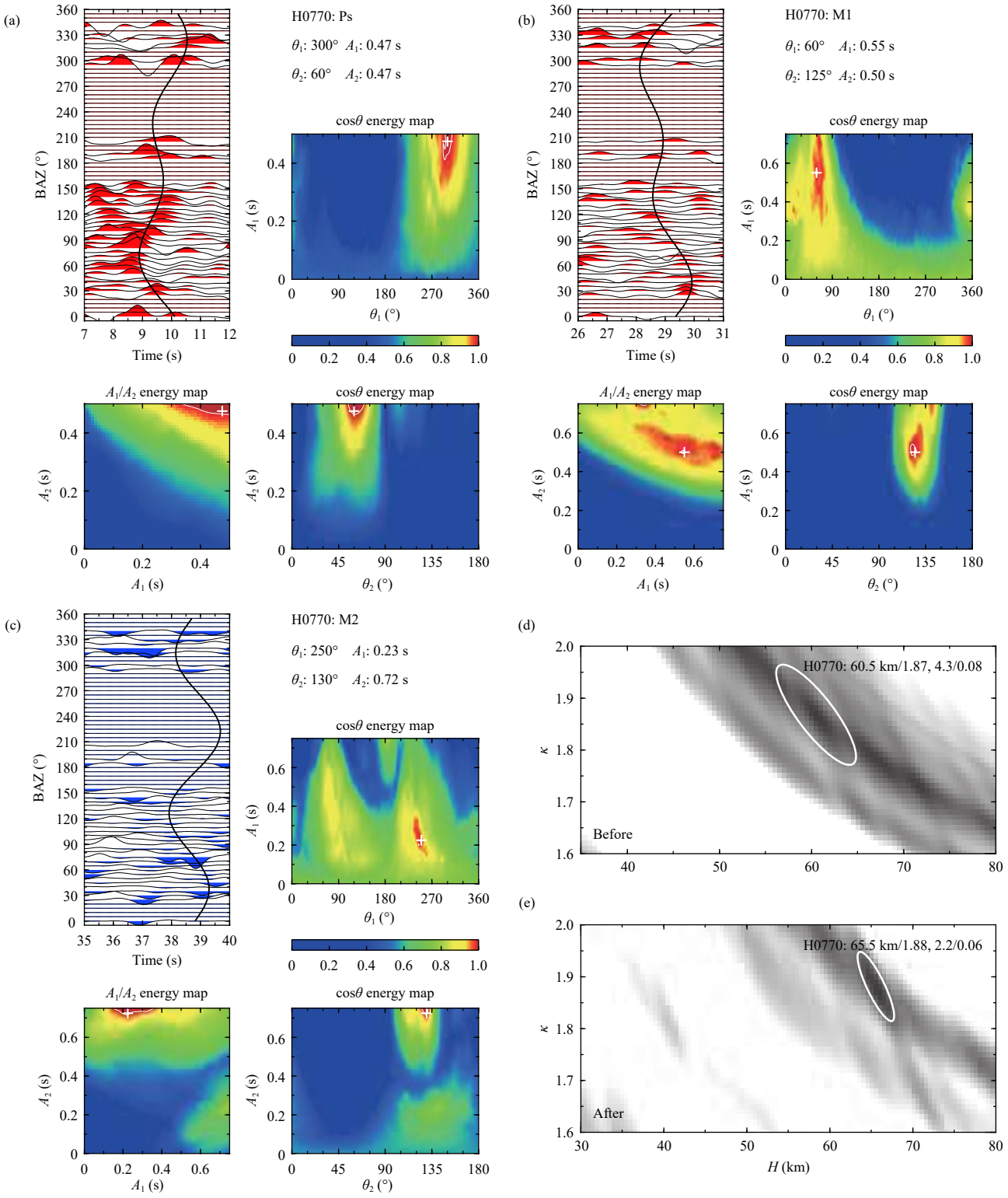

Figure 3. Similar layout to Figure 2 but for *H*-*κ*-c results on example station H0770. Note that the *H* range in (d) starts from 35 km to cut the unrealistic value in the corner.

significantly less scattered and are more consistent in trend, which demonstrates improvement by the *H*-*κ*-c method. This largely avoids unreasonable *H* estimates from traditional *H*-*κ* stacking. The smoothing splines for both measurements were calculated using a smoothing parameter of 0.9. The R-squared in spline fitting increases

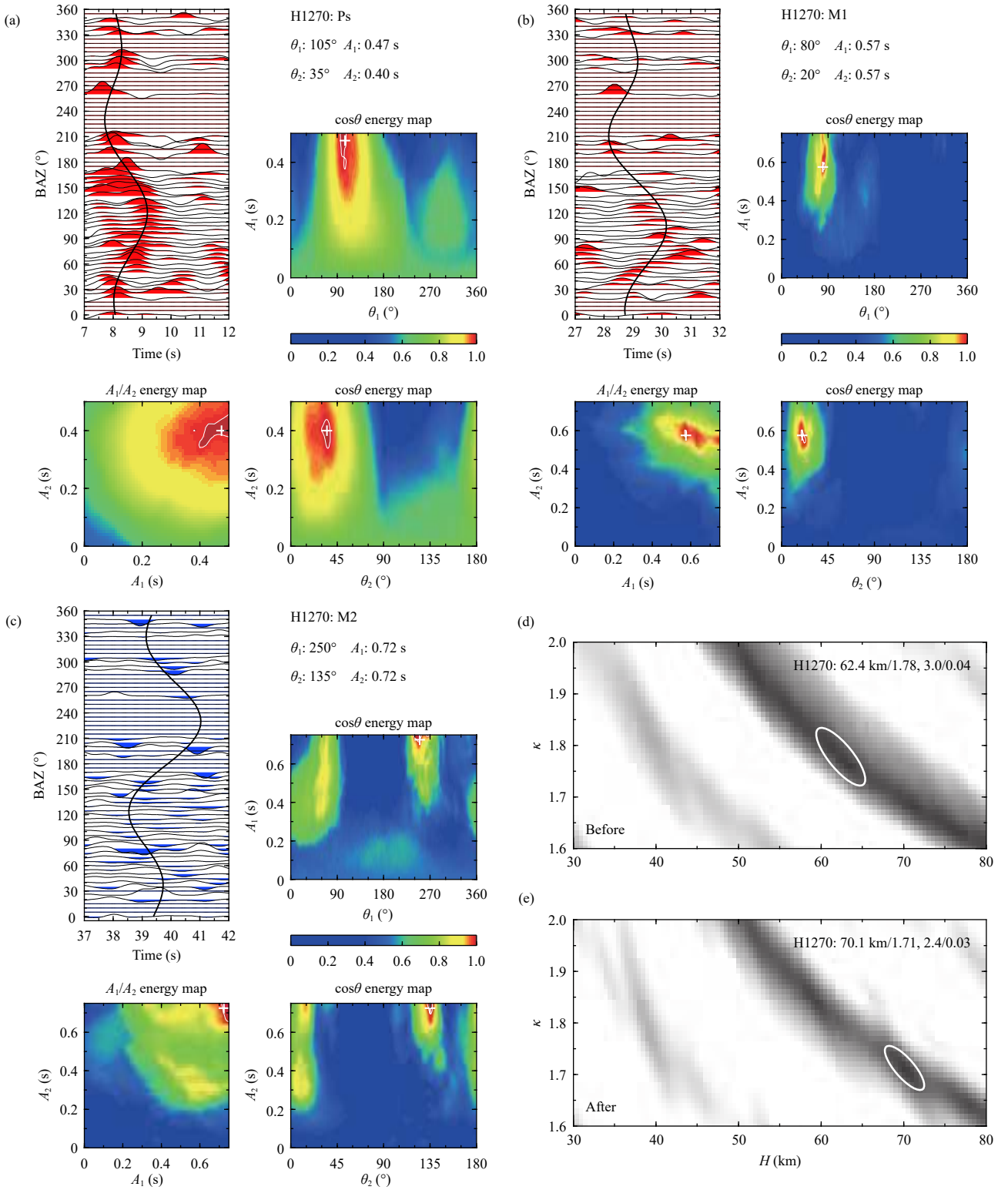

Figure 4. Similar layout to Figure 2 but for *H*-*κ*-c results on example station H1270.

from ~0.54 before corrections to ~0.83 after. The general trends appear similar, but there are apparent differences in the Lhasa and Qiangtang blocks. When considering the general agreement in thicker Lhasa crust and a northward thinning (e.g., Nábělek et al., 2009; Tseng et al., 2009; Wittlinger et al., 2009; Nowack et al., 2010; Xu ZJ et al., 2013a), the *H* after harmonic corrections should be more reliable.

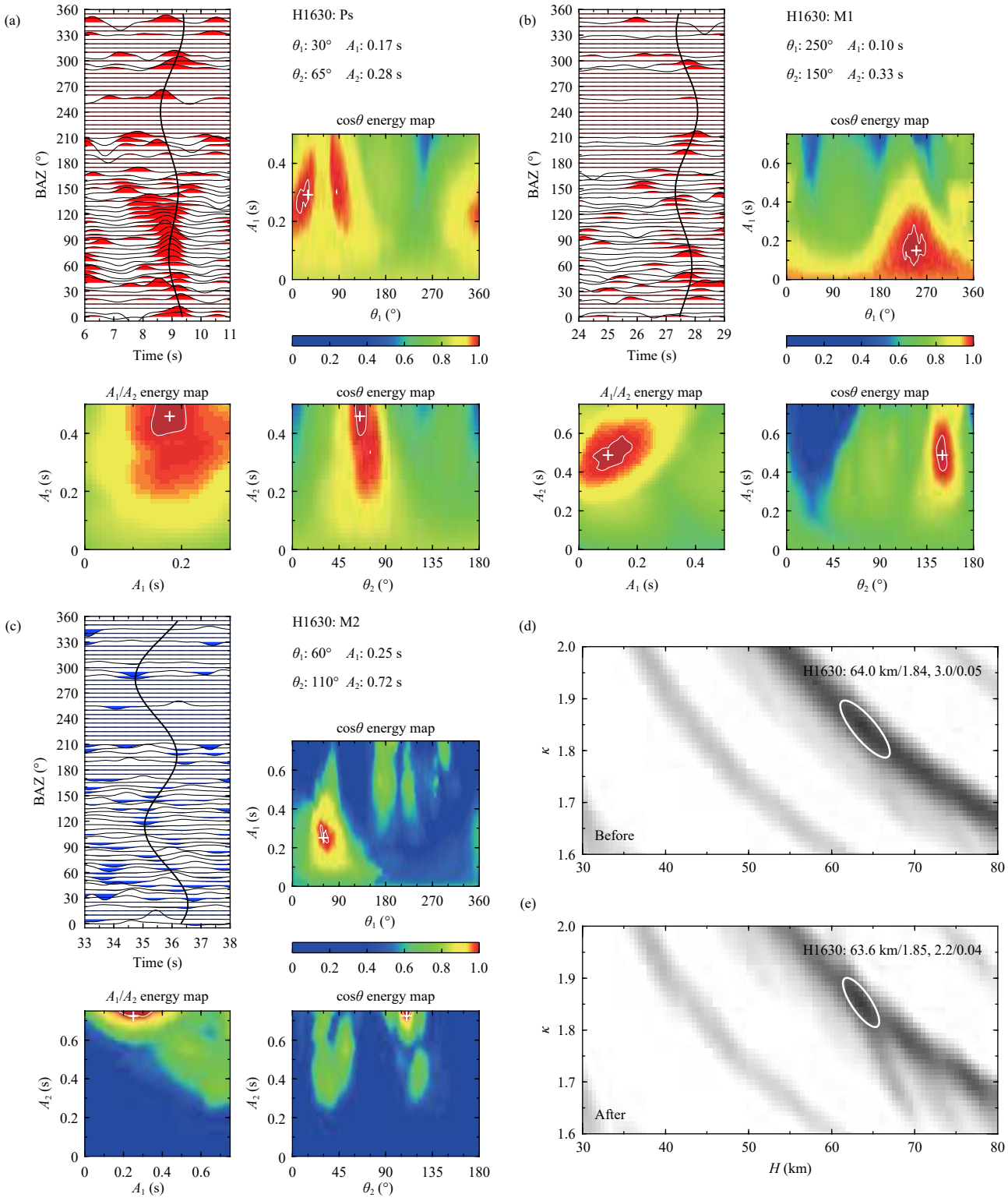

Figure 5. Similar layout to Figure 2 but for *H*-*κ*-c results on example station H1630. Note that the search ranges of A_1 and A_2 for Ps and M1 are limited to 0.3 and 0.5, respectively at this station, for the continuity of the arrivals.

The results were compared to those of Nábělek et al. (2009), who used the same Hi-CLIMB stations. Although the trend is similar, the *H* values differ. The average line (spline fit) of *H* from *H*-*κ*-c is shallower than that of Nábělek et al. (2009) beneath most of the TP. The line by Nábělek et al. (2009) resembles the outer boundary of the

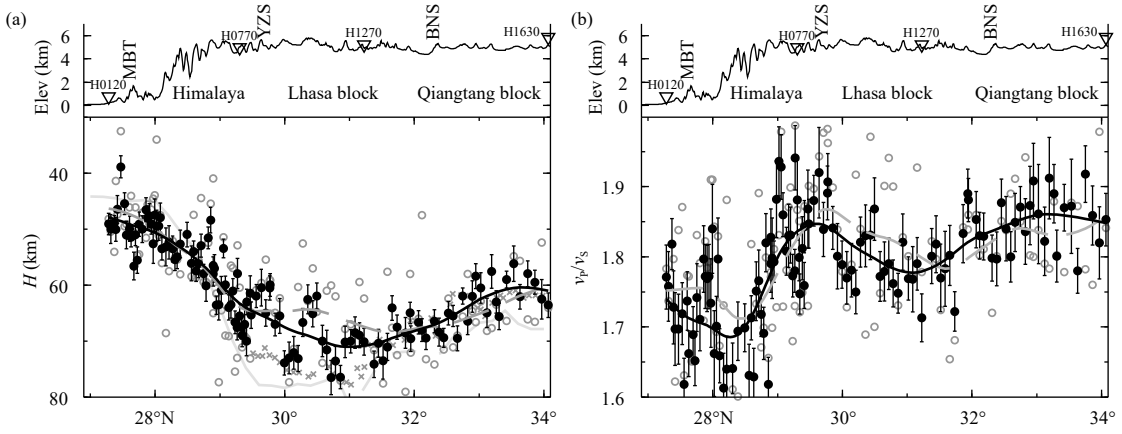

Figure 6. Results for crustal thickness (a) and v_P/v_S ratio (b) before, and after harmonic corrections, with smoothing spline fits along the Hi-CLIMB (122 stations). The results before are shown by gray circles and dark-gray dashed lines (its spline fit), and the results after are shown by black dots with error bars (standard deviations) and black lines (its spline fit). The thick light-gray line marks the approximated crustal thickness from Nábělek et al. (2009), with the dashed part indicating the location with weak Moho Ps conversion. Note that in Nábělek et al. (2009; their Figure 2) the Moho depth is relative to sea level, so here the topography is added to it. The gray crosses mark the crustal thickness estimated by SsPmp phase from Tseng et al. (2009). The topography is shown on top with blocks, main boundaries, and example stations labeled.

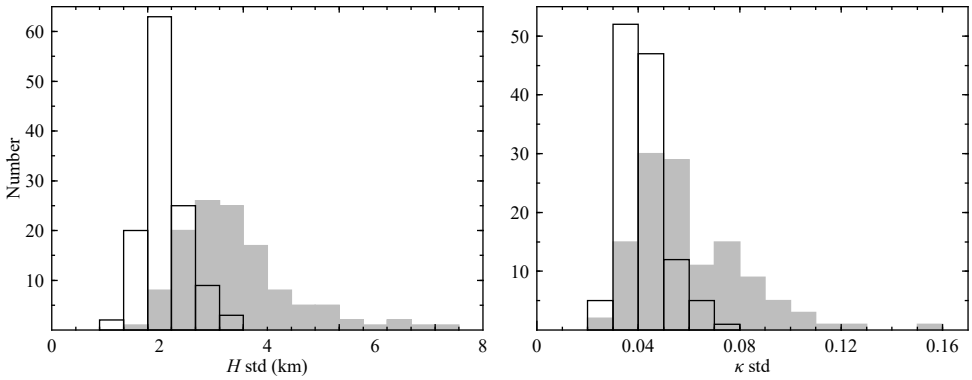

Figure 7. Histograms of the errors (standard deviation, std) of H and κ before (gray) and after (black) the harmonic corrections for the 122 Hi-CLIMB stations.

H measurements here. A possible reason for this is the difference in identifying the crustal multiples, especially M1 (PpPs), which could result in quite different H and κ estimates (Figure 4). The crustal multiples for stations in the TP are complicated and are greatly affected by crustal anisotropy and dipping layers, and therefore, may lead to different identifications and interpretations. The crustal v_P/v_S ratios in Nábělek et al. (2009) were mainly ~1.70–1.75 within the TP (their Supplementary Figure S3), with a gap at ~30.8°–33° N due to unclear Ps/M1 phases. However, in this study, the values in the TP are mostly larger than 1.75, and many of them are larger than 1.80 (Figure 6b). In view of the tradeoff between H and κ, a larger κ would correspond to a smaller H, as observed here, particularly for the large difference beneath the YZS where κ can be larger than 1.90. The results were also compared to the crustal thickness estimated by the SsPmp phase on Hi-CLIMB from Tseng et al. (2009; Figure 6a). The results are similar in the Qiangtang and northern Lhasa blocks, while the measurements in this study are shallower in the central and southern Lhasa block, which could be due to similar reasons above. Constraints from other independent datasets may be required to resolve this discrepancy. For example, a joint inversion of receiver function and surface wave dispersion with P-wave information, and possibly more constraints, will be helpful in this regard (e.g., Li JT et al., 2017; Ye Z et al., 2017, 2019; Deng YF et al., 2018, 2019). Conversely, Nábělek et al. (2009) observed weak Moho Ps conversion at ~31°–32.8° N (dashed part of their line), but here, it was found that many, if not most, of them do show a clear Ps phase after the harmonic corrections. Therefore, part of the observed weak conversions in Nábělek et al. (2009) may be an effect of complicated crustal anisotropy and/or

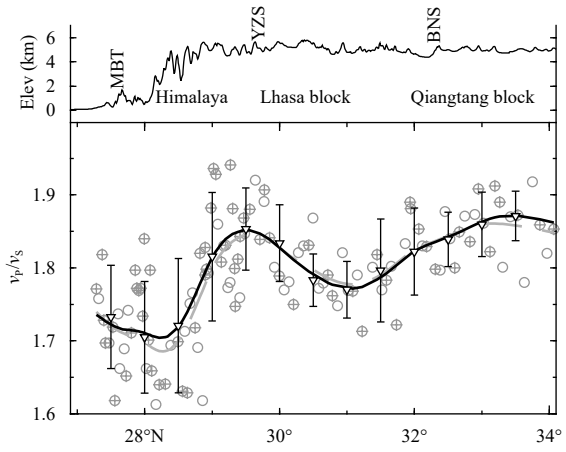

Figure 8. Crustal v_P/v_S measurements and spline fits for all 122 stations (gray circles and gray dashed line, same as the black dots and black line in Figure 6b) vs for the 70 selected stations with clear and consistent M1 arrivals (gray crosses, black line, and error bars). The error bar (± one standard deviation) is calculated within ±0.5° in latitude at each 0.5° grid, with the mean value shown by the triangle. The topography is shown on top with blocks and main boundaries labeled.

dipping layers in the TP.

The trend of variation in crustal thickness found here is similar to previous studies (e.g., Nábělek et al., 2009; Tseng et al., 2009; Wittlinger et al., 2009; Nowack et al., 2010; Xu ZJ et al., 2013a) of being thicker in the Lhasa block, and thinner in the Himalaya and Qiangtang blocks. The thinner crust in the northern TP is generally believed to be compensated by hot upper mantle materials following lithospheric delamination (Owens and Zandt, 1997; Tseng et al., 2009; Xu ZJ et al., 2013a). This hypothesis is supported by a series of surface wave tomography studies (e.g., Sun XL et al., 2010; Yang YJ et al., 2012; Xu ZJ et al., 2013b; Bao XW et al., 2015) that revealed an exceptionally low S velocity in the upper mantle beneath the Qiangtang block.

3.3. Crustal v_P/v_S ratio

Figure 6b summarizes the estimates of crustal v_P/v_S ratios (κ) before and after the harmonic corrections. It is clear that the κ values after corrections are also less scattered and relatively more consistent in trend compared to those from the traditional H-κ. The smoothing splines for both were also calculated with a smoothing parameter of 0.9. The R-squared in spline fitting increases from ~0.28 before corrections to ~0.57 after corrections. The general trends have some similarities, but the locations of the peaks and troughs differ. Here, only the fitting curve for the H-κ-c measurements was examined. In general, the v_P/v_S ratios beneath the high plateau (average > 1.80) are higher than those at low elevations (average ~1.70), revealing the difference between the Tibetan Plateau and the rigid Indian continent. Within the TP, there are two regions with relatively higher crustal v_P/v_S (averaged ~1.85), which are, one in the northern Himalaya block and beneath the YZS, and the other in the Qiangtang block. In the Lhasa block, the values are relatively lower (average ~1.80).

To determine whether the observed pattern is robust, all the harmonic fitting results of the M1 phase were rechecked. This was crucial for determining the crustal v_P/v_S. Among all the 122 stations used, it was found that some stations with very complex M1 may still have ambiguous solutions, even after careful inspections. Therefore, the stations with M1 arrivals that are either (1) strong and consistent (such as H0120 and H1630, could be the only solution), or (2) not quite strong, but clear and consistent (such as H0770 and H1270, the optimal solution with a few seconds) were selected. A final 70 stations were selected (Figure 8). Their spline fit, and the mean value and standard deviation within ±0.5° latitude at each 0.5° grid was calculated. The trend from the more robust measurements resembles that for all stations, suggesting that the measured crustal v_P/v_S variation should be reliable.

The two regions with relatively higher crustal v_P/v_S ratios correlate well with the two mid-crust low S velocity zones (LVZs) in Xu et al. (2013a) from joint inversion. As described by Xu ZJ et al. (2013a), the LVZ in the Himalaya block near the YZS can be over 25 km thick with a velocity reduction of more than 10%, but in the Lhasa block, both thickness and velocity reduction decrease significantly, and further north in the Qiangtang block, the amplitude of low velocity increases again. The two mid-crust LVZs along Hi-CLIMB have also been observed in recent surface wave tomography models (e.g., Yang YJ et al., 2012; Xu ZJ et al., 2013b; Bao XW et al., 2015; Huang SY et al., 2020). The correlation between high v_P/v_S ratio, low S velocity, and low electric resistivity (e.g., Unsworth et al., 2005) could suggest the presence of fluid or partial melt (Xu ZJ et al., 2013a), which may have implications for the crustal flow model. Conversely, the Lhasa block, judged by its relatively higher crustal S velocity (e.g., Xu ZJ et al., 2013a) and relatively lower crustal v_P/v_S (this study), should be mechanically stronger than the Himalaya and Qiangtang blocks, and possibly without partial melt in the crust.

4. Conclusions

In this study, the H-κ-c method (Li JT et al., 2019) was

applied to receiver function data on the Hi-CLIMB seismic array in the central-western Tibetan Plateau. The results indicate that it works well for regions with complex crustal structures, such as the TP, with helpful references from nearby stations on the array or other constraints. The improvements include greatly reduced errors, significantly less scattered H and κ values, more consistent and reliable crustal thickness, and clearer patterns of H and κ in different blocks, compared to the traditional H-κ method (Zhu LP and Kanamori, 2000).

The pattern of crustal thickness variation agrees with previous studies, but tends to be relatively shallower within most of the TP. Two regions with higher crustal v_P/v_S were observed, which were, one in the northern Himalaya block and beneath the YZS, and the other in the Qiangtang block. Their correlation with low S velocity patches in Xu ZJ et al. (2013a) suggests the possible presence of fluid or partial melt in the mid-crust of the two regions, and may have implications for the crustal flow model. In contrast, the Lhasa block has a relatively lower crustal v_P/v_S ratio and relatively higher crustal S velocity (Xu ZJ et al., 2013a) in the TP, which is interpreted to be mechanically stronger than the Himalaya and Qiangtang blocks, and possibly without partial melt in the crust.

Acknowledgments

We thank Lupei Zhu for providing the Hi-CLIMB receiver function data. The detailed constructive comments from three anonymous reviewers greatly improved the manuscript. The H-κ-c software is available from GitHub (https://github.com/ljt-uiuc/Hkc). Most figures were prepared using generic mapping tools (Wessel and Smith, 1998). This research was supported by the National Natural Science Foundation of China (No. 41774056) and the National Science Foundation of the United States (EAR 1620595).

References

Bao XW, Song XD, and Li JT (2015). High-resolution lithospheric structure beneath Mainland China from ambient noise and earthquake surface-wave tomography. Earth Planet Sci Lett **417**: 132–141.

Cassidy JF (1992). Numerical experiments in broadband receiver function analysis. Bull Seismol Soc Amer **82**(3): 1453–1474.

Chen WP, Martin M, Tseng TL, Nowack RL, Hung SH, and Huang BS (2010). Shear-wave birefringence and current configuration of converging lithosphere under Tibet. Earth Planet Sci Lett **295**(1-2): 297–304.

Clark MK, and Royden LH (2000). Topographic ooze: Building the eastern margin of Tibet by lower crustal flow. Geology **28**(8): 703–706.

Deng YF, Li JT, Song XD, and Zhu LP (2018). Joint inversion for lithospheric structures: Implications for the growth and deformation in Northeastern Tibetan Plateau. Geophys Res Lett **45**(9): 3951–3958.

Deng YF, Li JT, Peng TP, Ma Q, Song XD, Sun XL, Shen YS, and Fan WM (2019). Lithospheric structure in the Cathaysia block (South China) and its implication for the late Mesozoic magmatism. Phys Earth Planet Inter **291**: 24–34.

Duputel Z, Vergne J, Rivera L, Wittlinger G, Farra V, and Hetényi G (2016). The 2015 Gorkha earthquake: a large event illuminating the Main Himalayan Thrust fault. Geophys Res Lett **43**(6): 2517–2525.

England P, and Houseman G (1986). Finite strain calculations of continental deformation: 2. Comparison with the India-Asia collision zone. J Geophys: Res Solid Earth **91**(B3): 3664–3676.

Frederiksen AW, and Bostock MG (2000). Modelling teleseismic waves in dipping anisotropic structures. Geophys J Int **141**(2): 401–412.

Huang SY, Yao HJ, Lu ZW, Tian XB, Zheng Y, Wang R, Luo S, and Feng JK (2020). High-resolution 3-D shear wave velocity model of the Tibetan Plateau: Implications for crustal deformation and porphyry Cu deposit formation. J Geophys Res: Solid Earth **125**(7): e2019JB019215.

Klemperer SL (2006). Crustal flow in Tibet: a review of geophysical evidence for the physical state of Tibetan lithosphere. In: Searle MP, and Law RD (Eds) Channel Flow, Ductile Extrusion and Exhumation of Lower Mid-crust in Continental Collision Zones. Geol Soc Spec Publ **268**: 39–70.

Levin V, and Park J (1997a). Crustal anisotropy in the Ural Mountains foredeep from teleseismic receiver functions. Geophys Res Lett **24**(11): 1283–1286.

Levin V, and Park J (1997b). *P-SH* conversions in a flat-layered medium with anisotropy of arbitrary orientation. Geophys J Int **131**(2): 253–266.

Li JT, Song XD, Zhu LP, and Deng YF (2017). Joint inversion of surface wave dispersions and receiver functions with P velocity constraints: Application to Southeastern Tibet. J Geophys Res: Solid Earth **122**(9): 7291–7310.

Li JT, Song XD, Wang P, and Zhu LP (2019). A generalized H-κ method with harmonic corrections on *Ps* and its crustal multiples in receiver functions. J Geophys Res: Solid Earth **124**(4): 3782–3801.

Ligorria JP, and Ammon CJ (1999). Iterative deconvolution and receiver-function estimation. Bull Seismol Soc Amer **89**(5): 1395–1400.

Liu HF, and Niu FL (2012). Estimating crustal seismic anisotropy with a joint analysis of radial and transverse receiver function data. Geophys J Int **188**(1): 144–164.

Molnar P, and Tapponnier P (1975). Cenozoic tectonics of Asia: Effects of a continental collision. Science **189**(4201): 419–426.

Nábělek J, Hetényi G, Vergne J, Sapkota S, Kafle B, Jiang M, Su

HP, Chen J, Huang BS, and The Hi-CLIMB Team (2009). Underplating in the Himalaya-Tibet collision zone revealed by the Hi-CLIMB experiment. Science **325**(5946): 1371–1374.

Nowack RL, Chen WP, and Tseng TL (2010). Application of Gaussian-beam migration to multiscale imaging of the lithosphere beneath the Hi-CLIMB array in Tibet. Bull Seismol Soc Amer **100**(4): 1743–1754.

Owens TJ, and Zandt G (1997). Implications of crustal property variations for models of Tibetan plateau evolution. Nature **387**(6628): 37–43.

Powell CM (1986). Continental underplating model for the rise of the Tibetan Plateau. Earth Planet Sci Lett **81**(1): 79–94.

Royden LH, Burchfiel BC, King RW, Wang E, Chen ZL, Shen F, and Liu YP (1997). Surface deformation and lower crustal flow in eastern Tibet. Science **276**(5313): 788–790.

Royden LH, Burchfiel BC, and van der Hilst RD (2008). The geological evolution of the Tibetan Plateau. Science **321**(5892): 1054–1058.

Rümpker G, Kaviani A, and Latifi K (2014). *Ps*-splitting analysis for multilayered anisotropic media by azimuthal stacking and layer stripping. Geophys J Int **199**(1): 146–163.

Savage MK (1998). Lower crustal anisotropy or dipping boundaries? Effects on receiver functions and a case study in New Zealand. J Geophys Res: Solid Earth **103**(B7): 15069–15087.

Shang XF, de Hoop MV, and van der Hilst RD (2017). Common conversion point stacking of receiver functions versus passive-source reverse time migration and wavefield regularization. Geophys J Int **209**(2): 923–934.

Sun XL, Song XD, Zheng SH, Yang YJ, and Ritzwoller MH (2010). Three dimensional shear wave velocity structure of the crust and upper mantle beneath China from ambient noise surface wave tomography. Earthq Sci **23**(5): 449–463.

Tapponnier P, Xu ZQ, Roger F, Meyer B, Arnaud N, Wittlinger G, and Yang JS (2001). Oblique stepwise rise and growth of the Tibet Plateau. Science **294**(5547): 1671–1677.

Tseng TL, Chen WP, and Nowack RL (2009). Northward thinning of Tibetan crust revealed by virtual seismic profiles. Geophys Res Lett **36**(24): L24304.

Unsworth MJ, Jones AG, Wei W, Marquis G, Gokarn SG, Spratt JE, and The INDEPTH-MT Team (2005). Crustal rheology of the Himalaya and Southern Tibet inferred from magnetotelluric data. Nature **438**(7064): 78–81.

Wessel P, and Smith WHF (1998). New, improved version of generic mapping tools released. Eos **79**(47): 579–579.

Wittlinger G, Farra V, Hetényi G, Vergne J, and Nábělek J (2009). Seismic velocities in Southern Tibet lower crust: a receiver function approach for eclogite detection. Geophys J Int **177**(3): 1037–1049.

Xu Q, Zhao JM, Pei SP, and Liu HB (2011). The lithosphere-asthenosphere boundary revealed by *S*-receiver functions from the Hi-CLIMB experiment. Geophys J Int **187**(1): 414–420.

Xu ZJ, Song XD, and Zhu LP (2013a). Crustal and uppermost mantle S velocity structure under Hi-CLIMB seismic array in central Tibetan Plateau from joint inversion of surface wave dispersion and receiver function data. Tectonophysics **584**: 209–220.

Xu ZJ, Song XD, and Zheng SH (2013b). Shear velocity structure of crust and uppermost mantle in China from surface wave tomography using ambient noise and earthquake data. Earthq Sci **26**(5): 267–281.

Yang YJ, Ritzwoller MH, Zheng Y, Shen WS, Levshin AL, and Xie ZJ (2012). A synoptic view of the distribution and connectivity of the mid-crustal low velocity zone beneath Tibet. J Geophys Res: Solid Earth **117**(B4): B04303.

Ye Z, Li JT, Gao R, Song XD, Li QS, Li YK, Xu X, Huang XF, Xiong XS, and Li WH (2017). Crustal and uppermost mantle structure across the Tibet-Qinling transition zone in NE Tibet: Implications for material extrusion beneath the Tibetan plateau. Geophys Res Lett **44**(20): 10316–10323.

Ye Z, Li QS, Zhang HS, Li JT, Wang XR, Han RB, and Wu QY (2019). Crustal and uppermost mantle structure across the Lower Yangtze region and its implications for the late Mesozoic magmatism and metallogenesis, eastern South China. Phys Earth Planet Inter **297**: 106324.

Yin A, and Harrison TM (2000). Geologic evolution of the Himalayan-Tibetan orogen. Annu Rev Earth Planet Sci **28**: 211–280.

Yuan XH, Ni J, Kind R, Mechie J, and Sandvol E (1997). Lithospheric and upper mantle structure of southern Tibet from a seismological passive source experiment. J Geophys Res: Solid Earth **102**(B2): 27491–27500.

Zhang BF, Bao XW, and Xu YX (2020). Distinct orogenic processes in the South- and North-Central Tien Shan from receiver functions. Geophys Res Lett **47**(6): e2019GL086941.

Zhang PZ, Shen ZK, Wang M, Gan WJ, Bürgmann R, Molnar P, Wang Q, Niu ZJ, Sun JZ, Wu JC, Sun HR, and You XZ (2004). Continuous deformation of the Tibetan Plateau from global positioning system data. Geology **32**(9): 809–812.

Zhou YM (2013). Crustal structure of the Tibetan Plateau and its surroundings from receiver function studies. Dissertation, Saint Louis University.

Zhu LP, and Kanamori H (2000). Moho depth variation in southern California from teleseismic receiver functions. J Geophys Res: Solid Earth **105**(B2): 2969–2980.